Journal of Computational Physics **151,** 563–584 (1999)
Article ID jcph.1999.6197, available online at http://www.idealibrary.com on IDEAL®

An Efficient Method for the Solution of the Incompressible Navier–Stokes Equations in Cylindrical Geometries

M. Manna* and A. Vacca†

**Dipartimento di Ingegneria Meccanica per l'Energetica, Universitá di Napoli "Federico II," Naples, Italy;*
†*Dipartimento di Ingegneria Civile, Seconda Universitá di Napoli, Naples, Italy*
E-mail: manna@unina.it, vacca@unina.it

Received October 29, 1998; revised January 6, 1999

The article presents a fast pseudo-spectral Navier–Stokes solver for cylindrical geometries, which is shown to possess exponential rate of decay of the error. The formulation overcomes the issues related to the axis singularity, by employing in the radial direction a special set of collocation points together with standard Chebyshev polynomials. A multi-domain technique with patching interfaces yields significant improvements in the conditioning of the algebraic problems arising from the discretization procedure and allows for an enhanced near wall resolution of wall bounded shear flows. The elliptic kernel enjoys the efficiency of an analytic expansion of the harmonic extension. The method is tested by computing the formation of Taylor vortices in a rotating Couette flow for both axisymmetric and non-axisymmetric configurations. A direct numerical simulation of a turbulent pipe flow at moderate Reynolds number demonstrates the effectiveness of the method in as much as the axis singularity is concerned. Results compare well with reference experimental and numerical data.

Key Words: spectral methods; domain decomposition; cylindrical coordinates; turbulent flows.

1. INTRODUCTION

Thanks to the recent growth in computer hardware, we have been witnesses of an important shift from basic building block flows in simple geometries to more realistic configurations. However, many fundamental issues in the study of transition and turbulence of even very simple flows remain open and thus the interest for a comprehensive analysis tool is becoming more and more important. The simulation of turbulent flows requires the accurate resolution of all high frequency fluctuations associated to the small scales of turbulence. The quickly growing ratio of the integral to the dissipative scale with Reynolds number

0021-9991/99 $30.00

dictates severe resolution requirements for the direct numerical simulation (DNS) of even very low Reynolds number flows. As widely demonstrated by the open literature (see for instance [1] and references therein), spectral methods provide the most confident platform for a reliable turbulent data analysis, simply clearing out all possible doubts on the impact of the numerical scheme on the physics of the flow under investigation. This feature is not enjoyed by any other low order method. The higher computational cost of these methods is widely compensated by their fast (exponential) rate of convergence, as well as by their efficiency for long time integration problems.

Extensive developments are documented in the literature for Cartesian geometries, see [2] for a review, while in cylindrical coordinates, even for flows with two homogeneous directions, the available material is rather limited. The reason may be attributed to the additional difficulties which distinguish Cartesian flow problems from cylindrical ones, mainly the variable coefficients in the differential operators and the singularity in the coordinate system.

The first issue, which arises from the implicit treatment of the diffusive terms in the Navier–Stokes equations, precludes in fact the straight application of the "full step method" of Orszag *et al.* [3]. Leonard and Wray [4] introduced a new vector function in the expansion of the velocity field which is divergence free and satisfies the boundary conditions for viscous flow. They demonstrated, in a weighted residual context, spectral convergence on a linear stability problem using a special set of Jacobi polynomials. Priymak [5] succeeded in constructing a new algorithm without fractional steps where pressure values in the collocation points are eliminated from the discrete equations. The polynomial approximation in the r direction is either based on odd–even Chebyshev series with standard collocation nodes, or on Jacobi polynomials $P^{2,1}(r)$ with $r \in [-1, 1]$. In the latter case the spacing of the collocation points yields a reduced (compared to the former) resolution near the physical boundaries. This could represent a significant limitation for the simulation of turbulent flows where a correct prediction of the wall friction velocity is of paramount importance. All the above techniques have no splitting errors and thus appear very attractive; however, storage requirements in [4] and computational efficiency in view of the successive approximations method used in [5], render splitting methods more appealing for DNS of turbulent flows. The first application of a spectral technique employing a first order fractional step to investigate the behavior of finite amplitude disturbances in pressure driven pipe flow is due to Orszag and Patera [3]. As concerns the expansion in radial direction they used even or odd Chebyshev series which are compatible with the behavior of the variables at the origin. It is our belief that all of the above methods being *global* they cannot compete with their equivalent multi-domain counterpart. In fact domain decomposition principles not only alleviate the limitations of global methods allowing for more complicated flow simulations, but in addition they enable some sort of local refinements and thus increase the computational efficiency while maintaining the global (at domain level) rate of convergence. These features are probably all embodied in the spectral element technique of Patera [6]. Zhang *et al.* [7] carried out a direct numerical simulation of pipe flow at low to moderate Reynolds numbers with one dimensional spectral elements. In the element adjacent to the axis they used Lagrange interpolants based on the zeros of Jacobi polynomials $P^{0,1}(r)$ with associated weights which are zero at $r = 0$ and Legendre Lagrange interpolants elsewhere. The removal of the geometrical singularity is carried out applying Hopital's rule; by doing so they preserved the spectral convergence rate. We acknowledge that spectral elements, especially in their non-conforming version [8], represent the cornerstone for the simulation

of incompressible flows in complex geometries. Yet, they suffer from significant difficulties for large scale computing associated to the huge algebraic system resulting from the discretization. The development of well preconditioned iterative solvers constitutes, therefore, an essential feature of the method.

In this work we present an efficient and accurate multi-domain pseudo-spectral technique which, for turbulent flows with two homogeneous directions, is fully competitive, if not superior, to the spectral element method of [7]. We propose a simple and effective procedure to overcome the axis singularity based on the use of standard Chebyshev polynomials together with a special set of collocation points. The multi-domain technique, with patching interfaces, yields significant improvements in the conditioning of the algebraic problem arising from the discretization procedure. The elliptic kernel exploits the efficiency of an analytic expansion of the harmonic extension in terms of Bessel functions. The method is demonstrated to possess exponential rate of convergence on a domain basis not only for elliptic model problems, but also for the full Navier–Stokes equations. Validation is conducted computing the formation of Taylor vortices in a rotating Couette flow for both axisymmetric and non-axisymmetric configurations. Direct numerical simulation of turbulent pipe flow at moderate Reynolds number demonstrates the effectiveness of the method in coping with the axis singularity. This paper is organized as follows: in Section 2 we present the mathematical formulation and the temporal discretization of the Navier–Stokes equations. Section 3 covers the spatial discretization with particular emphasis on the domain decomposition and the treatment of the axis singularity. The same section demonstrates the exponential convergence rate of the elliptic kernel. Finally in Section 4 we check the accuracy of the Navier–Stokes algorithm for three different classes of test problems.

2. MATHEMATICAL FORMULATION

In this work we are concerned with the incompressible Navier–Stokes equations in their primitive variable form, although the mathematical and numerical formulation of the method applies to a more general set of partial differential equations. Let $\mathbf{x} = (z, r, \theta)^t$ and t be the space and time coordinates. The governing equations then read

$$\frac{\partial \mathbf{u}}{\partial t} = -\nabla p - \mathcal{N}\mathbf{u} + \frac{1}{Re}\mathcal{L}\mathbf{u}, \qquad \forall (\mathbf{x}, t) \in \Omega \times (0, T), \tag{1}$$

and

$$\nabla \circ \mathbf{u} = 0, \qquad \forall (\mathbf{x}, t) \in \Omega \times (0, T), \tag{2}$$

where $\mathbf{u} = (u, v, w)^t$ are the non-dimensional streamwise, radial, and azimuthal velocity components, p is the non-dimensional pressure, and Ω the physical domain with a smooth boundary $\partial\Omega$. The Reynolds number $Re = ul/\nu$ is based on the kinematic viscosity ν and an appropriate velocity and length scales (u and l).

Equations (1) and (2) are subject to a suitable set of boundary conditions,

$$\mathbf{u}(\mathbf{x}, t) = \mathbf{w}, \qquad \forall (\mathbf{x}, t) \in \partial\Omega \times (0, T), \tag{3}$$

and of initial conditions,

$$\mathbf{u}(\mathbf{x}, 0) = \mathbf{w}_0, \qquad \forall \mathbf{x} \in \Omega, \tag{4}$$

where $\nabla \circ \mathbf{w}_0 = 0$ in Ω.

The differential operators of (1) and (2) in cylindrical coordinates are given by

$$
\begin{aligned}
\nabla u &= \left(\frac{\partial u}{\partial z}, \frac{\partial u}{\partial r}, \frac{1}{r}\frac{\partial u}{\partial \theta}\right)^t,\\
\nabla \mathbf{u}\cdot\mathbf{n} &= \left(\nabla u\cdot\mathbf{n}, \nabla v\cdot\mathbf{n} - \frac{w n_\theta}{r}, \nabla w\cdot\mathbf{n} + \frac{v n_\theta}{r}\right)^t,\\
\nabla\circ\mathbf{u} &= \frac{\partial u}{\partial z} + \frac{1}{r}\frac{\partial r v}{\partial r} + \frac{1}{r}\frac{\partial w}{\partial \theta},\\
\Delta u &= \frac{\partial^2 u}{\partial z^2} + \frac{1}{r}\frac{\partial}{\partial r}\left(r\frac{\partial u}{\partial r}\right) + \frac{1}{r^2}\frac{\partial^2 u}{\partial \theta^2},\\
\mathcal{L}\mathbf{u} = \Delta\mathbf{u} &= \left(\Delta u, \Delta v - \frac{v}{r^2} - \frac{2}{r^2}\frac{\partial w}{\partial\theta}, \Delta w + \frac{2}{r^2}\frac{\partial v}{\partial\theta} - \frac{w}{r^2}\right)^t,\\
\nabla\times\mathbf{u} &= \left(\frac{1}{r}\frac{\partial r w}{\partial r} - \frac{1}{r}\frac{\partial v}{\partial\theta}, \frac{1}{r}\frac{\partial u}{\partial\theta} - \frac{\partial w}{\partial z}, \frac{\partial v}{\partial z} - \frac{\partial u}{\partial r}\right)^t.
\end{aligned}
\tag{5}
$$

In particular the non-linear convective term is computed in rotational form:

$$
\mathcal{N}\mathbf{u} = (\nabla\times\mathbf{u})\times\mathbf{u} + \frac{\nabla|\mathbf{u}|^2}{2}. \tag{6}
$$

Following the standard pressure correction approach we integrate the governing equations decoupling the velocity and the pressure at each time step [9]. To overcome the time step limitations of the diffusive operator we implicitly discretize the viscous terms (Crank–Nicolson); the convective operator is instead treated explicitly for simplicity (Adams–Bashforth). Let $\mathbf{u}^n$ be the approximation to $\mathbf{u}(\cdot, n\Delta t)$ at time level $n\Delta t$, and $\mathbf{v}$ the intermediate velocity vector field of the time splitting method whose curl $\nabla\times\mathbf{v}$ approximates $\nabla\times\mathbf{u}$ up to $\mathcal{O}(\Delta t)^2$. With these assumptions the semi-discrete form of (1), (2) reads

$$
\frac{\mathbf{v}-\mathbf{u}^n}{\Delta t} - \frac{1}{2Re}\Delta(\mathbf{v}+\mathbf{u}^n) = -\nabla p^n - \frac{3}{2}\mathcal{N}\mathbf{u}^n + \frac{1}{2}\mathcal{N}\mathbf{u}^{n-1}, \tag{7}
$$

$$
\frac{\mathbf{u}^{n+1}-\mathbf{v}}{\Delta t} = -\frac{1}{2}\nabla(p^{n+1}-p^n), \tag{8}
$$

$$
\nabla\circ\mathbf{u}^{n+1} = 0. \tag{9}
$$

The above formulation introduces a vortex sheet of strength $\mathcal{O}(\Delta t)^2$ at the boundaries which vanishes in the steady state.

Equations (7) constitute a set of coupled Helmholtz equations for the predicted velocity components; a scalar Poisson equation for the pressure follows from (8)–(9). Referring to the former set, for the sake of clarity, let us rewrite (7), as

$$
\alpha\mathbf{v} - \mathcal{L}\mathbf{v} = \mathbf{f}, \tag{10}
$$

where $\alpha = 2Re/\Delta t$ and $\mathbf{f}$ includes all known terms involved in (7). Unlike the Cartesian case, where the implicit treatment of the diffusion (together with the explicit treatment of the convection) still allows us to uncouple the momentum equations, in cylindrical coordinates the radial and azimuthal momentum equations are strongly coupled, as it can be easily

verified by inspection of (5). In the present work we assume the flow to be homogeneous in the azimuthal direction θ and thus we enjoy the computational efficiency of the fast Fourier transform by expanding in Fourier series all variables. The velocity field and the pressure are then represented in the transformed space by M_θ complex coefficients $\mathbf{v}_m$ and p_m as

$$\mathbf{v}(z,r,\theta,t) = \sum_{m=-M_\theta/2}^{M_\theta/2-1} \mathbf{v}_m(z,r,t)\, e^{im\theta} \qquad \forall\theta \in [0,2\pi], \tag{11}$$

$$p(z,r,\theta,t) = \sum_{m=-M_\theta/2}^{M_\theta/2-1} p_m(z,r,t)\, e^{im\theta} \qquad \forall\theta \in [0,2\pi]. \tag{12}$$

Introducing (11) in (10) and following the Galerkin projection method yields

$$\alpha\mathbf{v}_m - \hat{\mathcal{L}}\mathbf{v}_m = \mathbf{f}_m, \tag{13}$$

with

$$\begin{aligned}\hat{\mathcal{L}}\mathbf{v}_m = \Bigg(&\Delta_{rz}u_m - \frac{m^2}{r^2}u_m,\ \Delta_{rz}v_m - \frac{m^2+1}{r^2}v_m - \frac{2}{r^2}imw_m,\\ &\Delta_{rz}w_m - \frac{m^2+1}{r^2}w_m + \frac{2}{r^2}imv_m\Bigg)^t,\\ \Delta_{rz}\cdot = &\frac{\partial^2\cdot}{\partial z^2} + \frac{1}{r}\frac{\partial}{\partial r}\left(r\frac{\partial\cdot}{\partial r}\right).\end{aligned} \tag{14}$$

An analogous procedure is applied to the pressure Poisson equation.

This representation not only allows us to efficiently simulate a large class of turbulent flows, which are two dimensional in a statistical sense, but, as it will be shown below, it further provides the possibility of decoupling the diffusive terms. Let us begin observing that the coupling terms $2imw_m/r^2$ and $2imv_m/r^2$ of the r and θ complex components differ in sign, and thus a diagonalization of (14) can be obtained through a linear combination according to the following change of variables [3]:

$$\tilde{\mathbf{v}}_m = (\tilde{u},\tilde{v},\tilde{w})^t \equiv (u_m, v_m + iw_m, v_m - iw_m)^t. \tag{15}$$

Equation (13) then reduces to

$$\alpha\tilde{\mathbf{v}}_m - \tilde{\mathcal{L}}\tilde{\mathbf{v}}_m = \tilde{\mathbf{f}}_m, \tag{16}$$

where the scalar components of $\tilde{\mathbf{f}}_m$ obey analogous transformation as (15), and

$$\tilde{\mathcal{L}}\tilde{\mathbf{v}}_m = \left(\Delta_{rz}\tilde{u} - \frac{m^2}{r^2}\tilde{u},\ \Delta_{rz}\tilde{v} - \frac{(m+1)^2}{r^2}\tilde{v},\ \Delta_{rz}\tilde{w} - \frac{(m-1)^2}{r^2}\tilde{w}\right)^t. \tag{17}$$

Irrespective of the functional representation of the unknowns in the z, r directions, and disregarding the removable axis singularity, the above decomposition reduces, in a quite

general form, the original set of p.d.e. (7) to a cascade of two dimensional uncoupled elliptic problems, which do not differ from their Cartesian counterpart except for the explicit r-dependence of the differential operators. The class of problem investigated herein allows us to further exploit the Fourier transform procedure even in the z direction. Without loss of generality we can therefore represent the mth Fourier coefficient of the generic variable ϕ as

$$\phi_m(z, r, t) = \sum_{k=-M_z/2}^{M_z/2-1} \phi_{mk}(r, t)\, e^{i\beta kz}, \tag{18}$$

where the wave number $\beta = 2\pi/L_z$ is typically selected on physical ground, L_z being the length of the computational domain in the z direction. By doing so, we further simplify the p.d.e. (16) to a one dimensional problem. More precisely, again applying the Galerkin projection technique we are left with $M_z \times M_\theta$ uncoupled problems of the type

$$L\tilde{\mathbf{v}}_{mk} \equiv \left(\epsilon^2 + \frac{(m+\gamma)^2}{r^2}\right)\tilde{\mathbf{v}}_{mk} - \Delta_r \tilde{\mathbf{v}}_{mk} = \tilde{\mathbf{f}}_{mk}, \tag{19}$$

where

$$\Delta_r \cdot \equiv \frac{1}{r}\frac{\partial}{\partial r}\left(r\frac{\partial \cdot}{\partial r}\right), \tag{20}$$

with $\epsilon^2 = \alpha + (k\beta)^2$ and $\gamma = 0, 1, -1$ for the z, r, and θ components of the Helmholtz equations. The Poisson equation for the pressure follows from (19) setting $\alpha = \gamma = 0$, with obvious meaning of the source term $\tilde{f}_{mk}$.

3. NUMERICAL METHOD

As discussed in the Introduction domain decomposition methods partially alleviate the limitation of the global spectral method while at the same time enabling a local refinement which increases the computational efficiency. Let us consider a decomposition of the original domain $\Omega = (r_i, r_o)$ into an open set of M_d disjoint subdomains Ω_i ($\bar{\Omega} = \cup_{i=1}^{M_d} \bar{\Omega}_i$) inside each of which the solution satisfies the differential equation (19), that, for sake of clarity, we rewrite as

$$Lu = f \qquad \text{in } \Omega, \tag{21}$$

$$u = g_D \text{ on } \partial\Omega_D, \qquad \nabla u \cdot \mathbf{n} = g_N \text{ on } \partial\Omega_N, \tag{22}$$

with $\partial\Omega \equiv \partial\Omega_D \cup \partial\Omega_N$ and $\partial\Omega_D \cap \partial\Omega_N \equiv 0$; $\mathbf{n}$ the outwarding normal on $\partial\Omega$; L the elliptic operator (19); and f, g_D, and g_N the given data which are assumed to be smooth enough. Following [10], let us denote with λ the interface unknowns, defined on $\Gamma = (\bar{\Omega}/\cup_{i=1}^{M_d}\Omega_i)/\partial\Omega_D$. Using a linearity argument we decompose the solution u_i within each subdomain as

$$u_i \equiv w_i + v_i, \tag{23}$$

where the function w_i satisfies the inhomogeneous Dirichlet elliptic problem (hereafter denoted as Problem PI),

$$\begin{cases} L w_i = f_i & \text{in } \Omega_i, \\ w_i = g_D & \text{on } \partial\Omega_i \cap \partial\Omega_D, \\ w_i = 0 & \text{on } \partial\Omega_i \cap \Gamma, \end{cases} \tag{24}$$

and the "harmonic" extension of λ, v_i, satisfies the problem (hereafter denoted as Problem PH)

$$\begin{cases} L v_i = 0 & \text{in } \Omega_i, \\ v_i = 0 & \text{on } \partial\Omega_i \cap \partial\Omega_D, \\ \nabla v_i \cdot \mathbf{n} = g_N - \nabla w_i \cdot \mathbf{n} & \text{on } \partial\Omega_i \cap \partial\Omega_N, \\ v_i - v_j = 0 & \text{on } \partial\Omega_i \cap \partial\Omega_j \; i \neq j, \\ \nabla v_i \cdot \mathbf{n}_i + \nabla v_j \cdot \mathbf{n}_j = -(\nabla w_i \cdot \mathbf{n}_i + \nabla w_j \cdot \mathbf{n}_j) & \text{on } \partial\Omega_i \cap \partial\Omega_j \; i \neq j. \end{cases} \tag{25}$$

It is observed that the weak formulation of (25) leads to an entirely equivalent formulation in terms of the Steklov–Poincarè operator.

Having decoupled on a subdomain basis the original elliptic differential equation in two subproblems of reduced size, it is possible to exploit in a straightforward manner the parallel architecture of MIMD type machines. This is only true for Problem PI whereas Problem PH is necessarily sequential in nature. However, the cost associated to Problem PH will be shown to be marginal, thanks to the analytic solution procedure described below. The kind of finite dimensional approximation method which is used to solve the above problems is irrelevant to the present formulation.

Referring to Problem PI let us start with some notations. Let P_N be the space of algebraic polynomials of degree $\leq N$ with respect to the r variable. Moreover, let $\xi_k = \cos(\pi k/N)$, with $k = 0, \ldots, N$, the $N+1$ nodes of the Gauss–Lobatto–Chebyshev quadrature formula in the interval $[1, -1]$ [11]. It is straightforward to define a set r_k which is the image of the $N+1$ Lobatto points ξ_k by an affine transformation mapping $[1, -1]$ onto $\bar{\Omega}_i$, with $\bar{\Omega}_i \neq \bar{\Omega}_p \supset \{0\}$. The case Ω_p will be addressed later on. The discrete approximation of (24)–(25) is achieved following the so-called *patching collocation* method first introduced by Orszag [12]. Convergence estimates for both Chebyshev and Legendre polynomials, proving spectral rate of decay on each subdomain, can be found in [13]. In our framework and with reference to Problem PI, the above method consists in looking, within each subdomain, for a discrete function $w^N \in P_N$ satisfying

$$\begin{cases} L w^N = f^N & \text{in } \Omega_i, \\ w^N = g_D^N & \text{on } \partial\Omega_i \cap \partial\Omega_D, \\ w^N = 0 & \text{on } \partial\Omega_i \cap \Gamma. \end{cases} \tag{26}$$

The matrices arising from the algebraic systems (26) are full, albeit of small size, as discussed later; thus pivoted Gaussian elimination appears to be an attractive choice in view of the ill conditioned character of the matrices. For time dependent problems and in a parallel architecture environment, where core memory is not an issue, it is conceivable and most likely optimal to compute and store once in a preprocessing phase the LU factors, or alternatively to apply a diagonalization procedure. Incidentally we remark that the effect of

the variable coefficient in the operator L renders the application of the *tau* technique, which cost-wise is very attractive, not straightforward [3].

Turning to the homogeneous Problem PH and with reference to the operator L, we note that the harmonic extension w satisfies

$$r^2\frac{d^2w}{dr^2}+r\frac{dw}{dr}-(\epsilon^2r^2+m^2)w=0, \tag{27}$$

which, with the change of variables $x=r\epsilon$, reduces to the modified Bessel differential equation,

$$x^2w''+xw'-(x^2+m^2)w=0, \tag{28}$$

where the standard differentiation notation has been employed. Note that the term $(m+\gamma)^2$ in (19), with $\gamma=0, 1, -1$, is a non-negative integer, and thus, for sake of clarity, we can set $\gamma=0$. We recall that (28), because of the x^2 factor multiplying the second derivative, has a regular singularity at $x=0$. The solution of this o.d.e., for integer values of m, can be found in terms of the modified Bessel functions $I_m(x)$ and $K_m(x)$ of first and second kind, respectively,

$$w(x)=c_1I_m(x)+c_2K_m(x), \tag{29}$$

with

$$I_m(x)=\sum_{s=0}^{\infty}\alpha_s x^{2s+m}, \qquad K_m(x)=\log(x)I_m(x)+\sum_{s=0}^{\infty}\beta_s x^{2s-m}. \tag{30}$$

Obviously $K_m(x)$ is infinity at $x=0$, and thus to obtain a bounded solution we shall set $c_2=0$ in (29). The α_s and β_s values in (30) are readily obtained (with some lengthy, though straightforward, algebra) through the method of undetermined coefficients:

$$\alpha_s=(s!(s+m)!2^{m+2s})^{-1}, \qquad s=0,\ldots \tag{31}$$

$$\beta_s=\begin{cases}1/2^{2s-m+1}(-1)^{m-s-1}(m-s-1)!/s!, & s=0,\ldots,m-1\\ 0, & s=m\\ -1/2^{2s-m+1}1/(s-m)!1/s!\sum_{k=1}^{s-m}(1/k+1/(k+m)), & s=m+1,\ldots.\end{cases} \tag{32}$$

The coefficients (31) and (32) can be fast computed with the recursive formulae

$$\begin{aligned}\alpha_0&=(2^m m!)^{-1}\\ \alpha_s&=\alpha_{s-1}/[4s(s+m)], \qquad s=1,2,\ldots\end{aligned} \tag{33}$$

$$\begin{aligned}\beta_{m-1}&=2\alpha_0 m\\ \beta_{m-k}&=4(m-k+1)(1-k)\beta_{m-k+1}, \qquad k=2,\ldots,m\\ \beta_m&=0\\ \beta_{m+k}&=[\beta_{m+k-1}-2\alpha_k(2k+m)]/(4mk+4k^2), \qquad k=1,\ldots.\end{aligned} \tag{34}$$

In the case of the pressure Poisson equation, (27) can be directly integrated, in r variables, without resorting to generalized power series technique, for the constant mode $m=k=0$, to give

$$w(r)=c_1+c_2\log(r), \tag{35}$$

which degenerates to $w(r)=c_1$ when $\{0\}\subset\bar{\Omega}$. For each subdomain the constants c_1 and

c_2 are determined fulfilling the last four conditions in (25); more precisely the derivatives of w_i and w_j appearing in the right-hand sides are evaluated by the Chebyshev collocation differential operator, while the terms involving v_i and v_j are computed through (29) and (30). The $4(M_d-1)^2$ matrix of the resulting system in the case $\partial\Omega \equiv \partial\Omega_D$ is banded with an upper bandwidth 3.

Returning now to the issue of the removable axis singularity we recall that requiring the physical variables to be single valued at $r=0$ leads to the appropriate *pole condition*, which for both scalar and vector quantities is expressed imposing that the azimuthal derivatives must vanish at the origin [14]. Irrespective of the approximation used in the radial direction the pole condition must be accounted for when $\{0\} \subset \bar{\Omega}$ (see among many other [15, 16]). Ignoring it may give birth to significant degradations of the convergence properties of the spectral representation, and possibly, to instabilities [17].

There are several proposals for the application of Chebyshev expansion in the collocation framework available in literature. A direct mapping of the quadrature points in Ω has the advantage of clustering many points near the origin which may be useful for certain physical problems although $r=0$ is not a physical boundary. Also, one can expand the unknown variables in even or odd series which allows to keep a regular spacing of the collocation points at $r=0$. In the latter case the parity of the expansion must be compatible with the behavior of the solution at the origin [3, 5]. Inspecting (30) it is observed that the leading behavior of $\tilde{\mathbf{v}}$, as $r \to 0$, is

$$\tilde{\mathbf{v}}_m \sim (r^{|m|}, r^{|m+1|}, r^{|m-1|})^t. \tag{36}$$

Thus it is possible to incorporate the decay of the solution multiplying each of the polynomials by the appropriate power of r [3], which improves the accuracy. Although, with such a refinement, the expansions in even or odd Chebyshev series automatically satisfy the pole condition, they are not well suited for pure collocation methods since, for $m>1$ (i.e., non-axisymmetric problems), they require different collocation points for even and odd m modes [1]. The approach followed herein is based instead on standard orthogonal polynomial expansion ($p^N \in P_N$) in $[1,-1[$ combined with Gauss–Radau quadrature points. These nodes arise from the requirement of imposing boundary conditions at one end point (e.g., $x=1$), solely. This is achieved by determining the roots of the polynomial $q(x)=p^{N+1}(x)+ap^N(x)$, where $a=-p^{N+1}(1)/p^N(1)$ is chosen such that $q(1)=0$. In the case of Chebyshev series explicit formulae for the quadrature points are available: $\eta_k = \cos(2\pi k/(2N+1))$ with $k=0,\ldots,N$. Obviously in a multi-domain context an affine transformation mapping $[1,-1[$ onto $\bar{\Omega}_p/\{0\}$ is required. Using this set of collocation points there is no need to impose any boundary condition at the origin, and additionally it provides enhanced resolution close to $r=0$. In what follows we will show that the exponential properties of this spectral approximation are retained for elliptic problems even in presence of a nonlinear source term. Let us consider the numerical solution of the problem

$$r^2\frac{d^2u}{dr^2}+r\frac{du}{dr}-(\epsilon^2r^2+m^2)u = f, \qquad r\in\Omega=[r_i,r_o], \tag{37}$$

with $m=\epsilon=1$ and

$$f(r)=e^r\left\{\left[r-\left(\frac{2\pi r}{r_o-r_i}\right)^2-1\right]\cos\frac{2\pi(r-r_i)}{r_o-r_i}-\left(\frac{2\pi r}{r_o-r_i}\right)(2r+1)\sin\frac{2\pi(r-r_i)}{r_o-r_i}\right\}, \tag{38}$$

TABLE I

$\mathcal{L}_\infty$ Norm of the Error for Eq. (37) with $M_d = 3$

N	$N \times M_d$	Case 1	Case 2
4	12	1.62×10^{-2}	6.42×10^{-2}
6	18	3.80×10^{-4}	1.40×10^{-3}
8	24	3.25×10^{-6}	1.16×10^{-5}
10	30	1.42×10^{-8}	4.93×10^{-8}
12	36	3.85×10^{-11}	1.23×10^{-10}
14	42	2.27×10^{-14}	7.45×10^{-14}

for which the analytic solution $u(r) = e^r \cos(2\pi(r - r_i)/(r_o - r_i))$ exists. Since all data and u are analytic we expect exponential convergence to the exact solution, for a fixed number of subdomains, as the number of collocation points is increased. Let us start comparing the behavior of the error in the presence (Case 1, $\Omega = [0, 3]$) and absence (Case 2, $\Omega = [1, 4]$) of axis singularity. The boundary conditions are Neumann at $r = r_o$ and Dirichlet at $r = r_i$ for Case 2, while only one boundary condition (Neumann at $r = r_o$) is prescribed for Case 1. We consider three equally sized subdomains with the same number of points in each. Table I shows, for both cases, that when the resolution is doubled the relative error in the $\mathcal{L}_\infty$ norm is more than squared (exponential decay). Table II indicates, instead, that the error decay is algebraic with the number of subdomains. Thus no special effort is required to approximate the radial derivatives in the presence of the singularity when standard orthogonal polynomials are combined with the Gauss–Radau collocation points. Furthermore, the peculiarities of classical pseudo-spectral methods in Cartesian coordinates are retained both in terms of storage and accuracy, despite the additional difficulties associated with the cylindrical differential operators. Finally, the analytic expansion of the harmonic extension renders the proposed technique very appealing even in terms of computational efficiency. Although the above results are based on a simple model problem they nevertheless are representative of more complex situations recalling that for the Navier–Stokes equations the implicit treatment of the diffusive terms is the prevailing part. The main conclusions which can be drawn, at least in qualitative manner, are that when the required accuracy is increased, it may be more convenient to augment the number of collocation nodes rather than the number of subdomains. The opposite is true for those class of problems where accuracy is not a major issue. However, one must keep in mind that the computational cost of the elliptic kernel in three dimensions scales, roughly speaking, with $M_z \times M_\theta \times M_d \times N^h$, where h reduces from 3 to 2 if the LU factors are stored in a preprocessing stage. Thus from a computational cost

TABLE II

$\mathcal{L}_\infty$ Norm of the Error for Eq. (37) with $N = 10$

M_d	$N \times M_d$	Case 1	Case 2
1	10	4.22×10^{-5}	1.67×10^{-4}
3	30	1.42×10^{-8}	4.93×10^{-8}
5	50	2.21×10^{-10}	7.61×10^{-10}
7	70	1.44×10^{-11}	5.00×10^{-11}
9	90	1.70×10^{-12}	6.61×10^{-12}

point of view it is tempting to keep N to moderate values and to rise M_d. These conflicting issues have to be compromised somehow and no general rules to simulate complicated flow structures can be stated. Our experience indicates that DNS of turbulent pipe flow at moderate Reynolds number can be accurately carried out with $N \approx 12$ and $M_d \approx 6$. These features are shared by the one dimensional spectral element discretization of Zhang *et al.* [7], which, for the class of problem investigated herein, appears less efficient in as much as the treatment of the elliptic operators is concerned. Comparing the cost of the present method with the single domain approach of Priymak [5], who also solved turbulent pipe flows, we claim a better efficiency with equal spatial resolution.

4. RESULTS

Hereafter we present numerical results for 3 test problems which clearly demonstrate the potential of the Navier–Stokes solver. Whenever possible we have used analytical solutions or reference numerical and experimental data for the sake of comparison.

4.1. *Swirling Flow in Annular Pipe*

This test case has been selected in order to verify the ability of the present method to simulate, in the Navier–Stokes framework, steady flows which admit analytical solution, with both axial and azimuthal velocity distributions. To this aim let us consider the fully developed flow in the annular region between two coaxial circular cylinders whose inner and outer radii are r_i and r_o, respectively. The relevant non-dimensional parameter is defined as $Re = u_b\, 2\, r_o(1-\eta)/\nu$, where u_b represents the bulk (area averaged) axial velocity and $\eta = r_i/r_o$. The analytic solution for laminar flow conditions, which occur as long as $Re < 2000$, is easily found through momentum balance,

$$u_a(r) = 2u_b \frac{(1-(r/r_o)^2)\log\eta - (1-\eta^2)\log(r/r_o)}{(1+\eta^2)\log\eta + (1-\eta^2)}, \qquad v_a = w_a = 0. \tag{39}$$

In addition if the inner cylinder rotates at constant angular velocity ω about the z axis, and the associated Taylor number ($Ta = \omega\, r_i r_o(1-\eta)/\nu$) does not exceed a critical value [18], the whole motion consists of a superposition of (39) with

$$u_a = v_a = 0, \qquad w_a(r) \;=\; \omega r_i \frac{\eta}{1-\eta^2}\left[\frac{r_o}{r} - \frac{r}{r_o}\right]. \tag{40}$$

Expressing u_b in terms of Re and of the pressure gradient, it is easy to verify that solution (39) reduces to the classical Hagen–Poiseuille formula as $\eta \to 0$. In Fig. 1 we give the computed streamwise and azimuthal normalized velocity components as a function of the non-dimensional radius $\xi = (r - r_i)/s$, with $s = r_o - r_i$, together with the analytical distributions, for $\eta = 0.5$ and $s = 1$.

We have carried out computations of this flow for several (N, M_d) pairs and reported in Tables III and IV the $\mathcal{L}_\infty$ norm of the error. The exponential error decay, for a fixed number of subdomains $M_d = 2$, and the algebraic character, for a fixed number of Chebyshev polynomials $N = 4$, is then confirmed even for the whole Navier–Stokes algorithm.

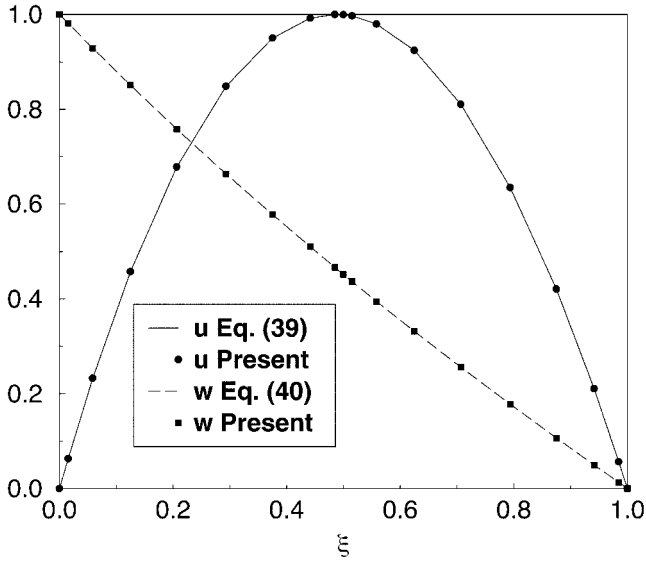

FIG. 1. Velocity components of swirling flow as a function of the non-dimensional radius.

4.2. *Taylor Vortex Flow*

We proceed in the validation of the method presenting in this section numerical solutions of the Taylor–Couette flow for both axisymmetric and non-axisymmetric conditions. This class of problems is known to represent a tough test-bench for all algorithms solving the Navier–Stokes equations as an initial value problem; as indicated in [19] these rotating flows are sensitive to the splitting errors because of the forcing term present at the radial boundaries. In [19] a special set of Green functions allowing to satisfy exactly the inviscid boundary conditions was found necessary to remove the time splitting errors. We shall attempt to give a numerical evidence of the quality of the present results comparing various integral and local quantities with the reference data of [20].

It is well known that several stable solutions of the Navier–Stokes equations governing the Taylor–Couette flow exist, depending essentially on the values of three independent dimensionless parameters: the radius ratio η, the axial wavelength λ_z, and the Reynolds number $Re = \omega r_i s/\nu$. In what follows we have used s as the unit length. For each pair (η, λ_z) there exists a critical value $Re_c(\eta)$ such that for $Re < Re_c$, (40) represents a stable solution of (1)–(2). For $Re > Re_c$, which in the narrow gap limit ($\eta \to 1$) can be estimated

TABLE III

$\mathcal{L}_\infty$ Norm of the Error for Swirling Flow with $M_d = 2$

N	$N \times M_d$	$\|\mathbf{u} - \mathbf{u}_a\|$
4	8	4.36×10^{-3}
6	12	6.21×10^{-5}
8	16	8.06×10^{-7}
10	20	1.00×10^{-8}
12	24	1.21×10^{-10}
14	28	1.76×10^{-12}

TABLE IV
$\mathcal{L}_\infty$ Norm of the Error for Swirling Flow with $N = 4$

M_d	$N \times M_d$	$\|\mathbf{u} - \mathbf{u}_a\|$
2	8	4.36×10^{-3}
4	16	1.32×10^{-3}
6	24	6.11×10^{-4}
8	32	3.50×10^{-4}
10	40	2.26×10^{-4}
12	48	1.58×10^{-4}

by eigenvalue analysis as $Re_c = 41.41(1 - \eta)^{-0.5}$, the circular Couette flow is unstable to three dimensional axisymmetric Taylor vortices. The latter appear as counter-rotating toroidal vortices aligned along the z axis. At still higher Reynolds number Taylor vortex flow is itself unstable to non-axisymmetric disturbances with several possible azimuthal wavelengths. These flows are three dimensional and unsteady in general, although for the one travelling wave case a proper choice of a rotating frame renders the flow steady [19]. We have computed both steady axisymmetric Taylor vortex flow and non-axisymmetric wavy vortex flow with one travelling wave. The initial conditions for the Taylor vortex flow were obtained perturbing the circular Couette flow with infinitesimal axisymmetric disturbances. Similarly the one travelling wave solution was obtained perturbing the Taylor vortex flow with non-axisymmetric disturbances. All calculations were carried out with 4 subdomains each of which consisted of 12 Chebyshev polynomials and 32 axial Fourier modes. In the non-axisymmetric case 32 azimuthal Fourier modes were employed. The subdomains adjacent to the inner and outer walls were characterized by a radial extension equal to $s/8$ to enhance the resolution of the near wall gradients. The time step was set to 0.01.

We begin the analysis reporting several integral parameters of physical quantities, per unit axial length, that characterize the different flow regimes, namely kinetic energy, angular momentum, enstrophy, and torque. They obey the usual definitions:

$$E = \int_0^{2\pi} \int_0^{L_z} \int_{r_i}^{r_o} |\mathbf{u}|^2 r \, dr \, dz \, d\theta, \tag{41}$$

$$\mathcal{L} = \int_0^{2\pi} \int_0^{L_z} \int_{r_i}^{r_o} w r^2 \, dr \, dz \, d\theta, \tag{42}$$

$$\mathcal{E} = \int_0^{2\pi} \int_0^{L_z} \int_{r_i}^{r_o} |\nabla \times \mathbf{u}|^2 r \, dr \, dz \, d\theta, \tag{43}$$

$$G_o = \int_0^{2\pi} \int_0^{L_z} r_o^2 \frac{\partial w}{\partial r}\bigg|_{r=r_o} dz \, d\theta. \tag{44}$$

In Table V we compare the computed values for axisymmetric Taylor vortex flow ($\eta = 0.875$, $Re = 140$, $\lambda_z = 2.5$) and non-axisymmetric one travelling wave flow characterized by a fundamental azimuthal wave number equal to 6 ($\eta = 0.868$, $Re = 230$, $\lambda_z = 2.14$) with the reference data of [20]. Despite the subtleties of the Taylor–Couette flow conditions, the quality of the results indicates that the proposed method represents a valid alternative to the use of Green function technique suggested in [19].

TABLE V
Summary of Physical Properties for Taylor Vortex Flow and One Travelling Wave Flow

	Taylor vortex		One travelling wave	
	Present	Data from [20]	Present	Data from [20]
E	7.14	7.14	6.13	6.13
$\mathcal{L}$	163	163	142	142
G_o	3.35	3.35	2.71	2.71
$\mathcal{E}$	27.0	27.1	41.0	41.2

In Fig. 2 we give the axially and azimuthally averaged non-dimensional angular momentum $rw/(\omega r_i^2)$ as a function of ξ for both the axisymmetric (unstable) Taylor Vortex flow and the non-axisymmetric one travelling wave flow characterized by an azimuthal wave number equal to 6 ($\eta = 0.875$, $Re = 244$, $\lambda = 3.0$). The computed results are again compared with the data of [20]. Note that the angular momentum of the stable one travelling wave flow exhibits a smaller gradient at the boundaries compared with the unstable Taylor vortex flow. Also the flattening of rw in the core region is related to the larger momentum transfer. Keeping in mind that the error decay is exponential with N and algebraic with M_d (see Subsection 4.1), we remark that the excellent agreement of our calculations with the spectral single domain of [19] is to be attributed to the flexibility of the present method. In fact the rates at which angular momentum and energy leave or enter the cylinder are proportional to the viscosity and to the gradient velocity at the boundaries; thus any numerical calculation must correctly resolve the near wall regions, which in the framework of spectral multi-domain methods can be accomplished through a proper choice of the subdomain's height and the number of points independently.

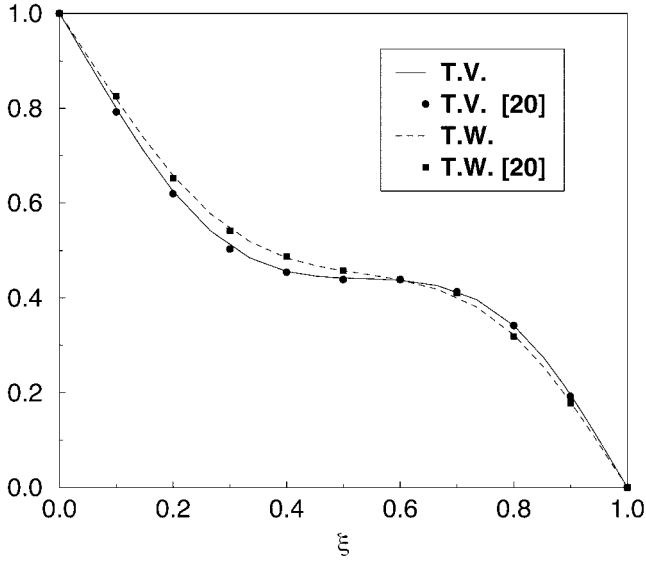

FIG. 2. Angular momentum as a function of the non-dimensional radius: Taylor vortex (T.V.) and one travelling wave (T.W.).

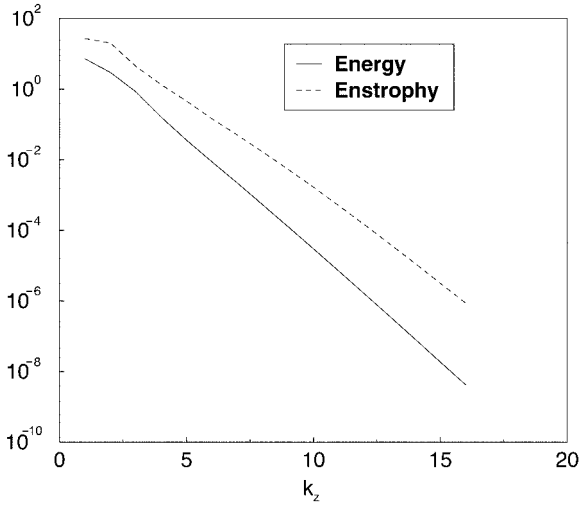

FIG. 3. Energy and enstrophy spectra as a function of the axial wave number k_z for Taylor vortex flow.

In Fig. 3 the one dimensional energy and enstrophy spectra are depicted as a function of the axial wave number k_z for the Taylor vortex flow ($\eta = 0.875$, $Re = 140$, $\lambda_z = 2.5$). We note that both $E(k_z)$ and $\mathcal{E}(k_z)$ obey a rate of fall off as e^{-k_z} and are very smooth as demonstrated by [20]. Also, the absence of any upward curl in the spectra at large wave numbers indicates the adequacy of the spatial resolution.

In Fig. 4 we show the azimuthal velocity component isolines together with the velocity vectors, for both the Taylor Vortex and the one travelling wave flows. The previously mentioned flattening of rw in the gap core is clearly related to a more intense vortical activity. Note that the boundary layers in the cross plane are substantially fuller for the one travelling wave flow.

4.3. *Direct Numerical Simulation of Pipe Flow*

We have computed a fully developed turbulent pipe flow at a Reynolds number of 2500 based on bulk velocity u_b and pipe diameter $D = 2R$, to assess the ability of the method in dealing with complicated flow structures as well as to demonstrate the effectiveness of the pipe axis treatment. The length of the pipe ($L_z = 8R$) is chosen long enough to include the largest scale structures in the flow. The computation was carried out with 442,368 grid points (6 subdomains each of which consisted of $12 \times 64 \times 96$ points in radial, circumferential, and streamwise directions, respectively). With this configuration the minimal r value at the pipe axis was 3.94×10^{-4}. The radial extent of the near wall subdomain was adjusted in such a way that the first mesh point away from the wall is located at $r^+ = (R - r)u_\tau/\nu = 0.1$ where $u_\tau = (\tau_w/\rho)^{0.5}$ is the wall shear velocity. Our streamwise grid-spacing Δz^+ is 7.7 wall units, while the circumferential one $r\,\Delta\theta^+$ varies linearly with r, from a maximum value of 9.1 at the pipe wall, to 0.01 at the pipe axis. This resolution is comparable both to the one used by Eggels *et al.* [21] in their pipe flow simulation (1.9, 8.8, 7 in r, θ, z directions), and by Kim *et al.* [22] in their plane channel (2.8, 7, 12 normal to the wall, span-wise, and streamwise directions, respectively). Computing the mean grid size $\Delta^+ = (\Delta r^+ r\,\Delta\theta^+\,\Delta z^+)^{1/3}$ we have checked that the resolution is sufficient to resolve all relevant turbulent scales, almost down

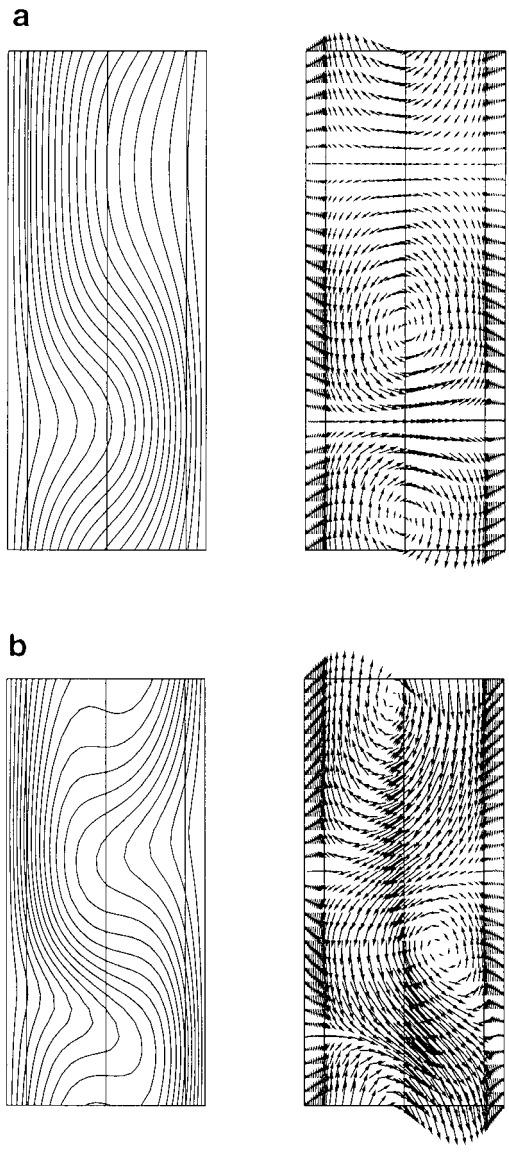

FIG. 4. Azimuthal velocity contours (contour level $\Delta = 0.05$) and velocity vectors: Taylor vortex flow (a) and travelling wave flow (b).

to the Kolmogorov scale η^+, for which estimates were given in [23]. The time step was set to $\Delta t = 5 \times 10^{-3}$.

The initial velocity field has been created superposing to a logarithmic distribution random noise with a prescribed standard deviation. The steady state is identified by a constant time averaged wall shear stress, and by a quasi periodic turbulent kinetic energy. The sample size used to collect statistics is roughly 14 non-dimensional time units $t^+ = tu_\tau/D$. In Fig. 5 we present the energy spectra of all velocity components, normalized with the friction velocity, at two different radial locations, namely $r^+ \approx 10$ and $r^+ \approx 90$. The spectra are presented as a function of the streamwise wave number $k_z = 2\pi k/L_z$. The drop in the energy of several orders of magnitude and the absence of pile up at the highest wave number clearly reveal

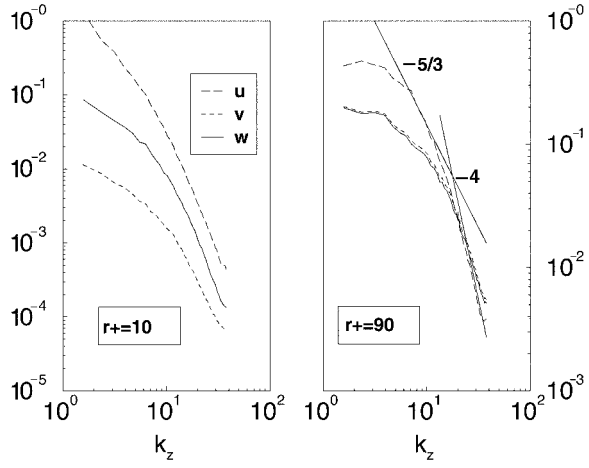

FIG. 5. One dimensional energy spectra.

that the simulation is "resolved" in the sense described above. In particular the distinction between the range of dissipative scales and the energy containing motions is rather neat at $r^+ \approx 90$, as confirmed by the resemblance of the computed spectra with the k^{-4} and $k^{-5/3}$ slopes. The reduced extent of the inertial sub-range agrees with theoretical arguments stating that a sufficiently wide separation between the largest and smallest eddies is only present when the turbulent Reynolds number, based on Taylor micro-scale Re_λ, is larger than 2000. Starting from the streamwise correlation coefficient R_{uu} we have estimated Re_λ to be of order 100. The computed skin friction coefficient $C_f = \tau_w/(0.5\rho {U_b}^2) = 11.13 \times 10^{-3}$ is in very good agreement with the Blasius law $C_f = 0.079 Re^{-0.25} = 11.19 \times 10^{-3}$.

In Fig. 6 we present the mean velocity profile normalized by the centerline velocity together with the experimental data of Patel and Head [24] and those of Zhang *et al.* [7]. The

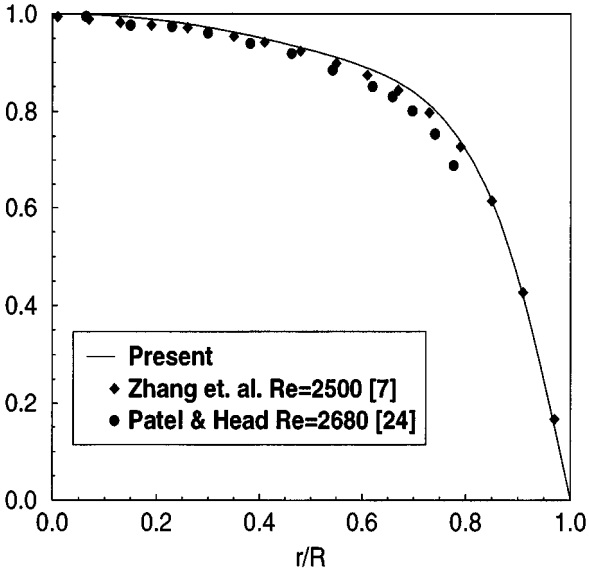

FIG. 6. Streamwise mean velocity profiles in outer coordinates.

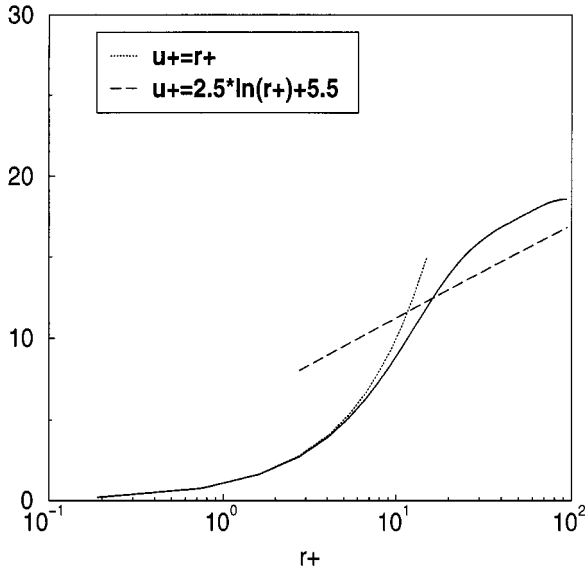

FIG. 7. Streamwise mean velocity profiles in inner coordinates.

DNS data, which agree well among themselves, suggest fuller velocity profiles compared to the experiments. In Fig. 7 the mean velocity profile is given in inner variables, together with the law of the wall and the logarithmic one. It is observed that the viscous sublayer is completely resolved by the simulation, while important deviations from the universal profile distribution are present for $r^+ > 10$. This trend agrees with the observations of Patel and Head [24] who demonstrated that low Reynolds number pipe flows ($Re \leq 10^4$) fail to conform to the law of the wall. In Fig. 8 we present the turbulent intensities of all velocity components normalized with the theoretical value of the shear velocity. The agreement

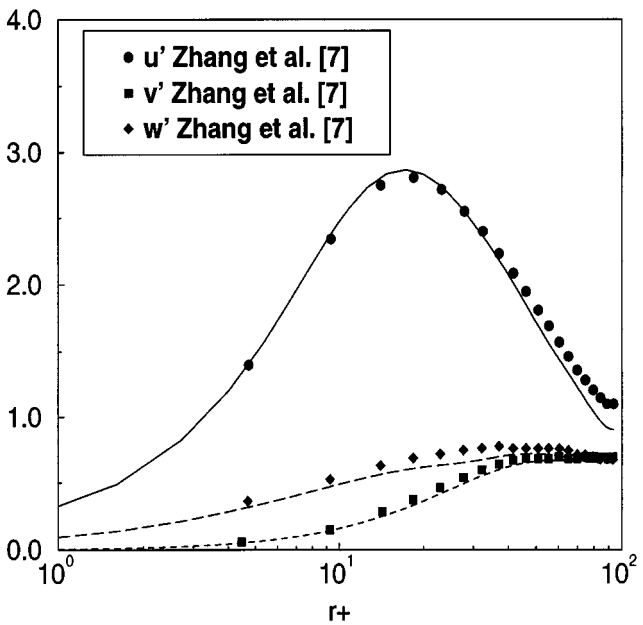

FIG. 8. Normal stress components.

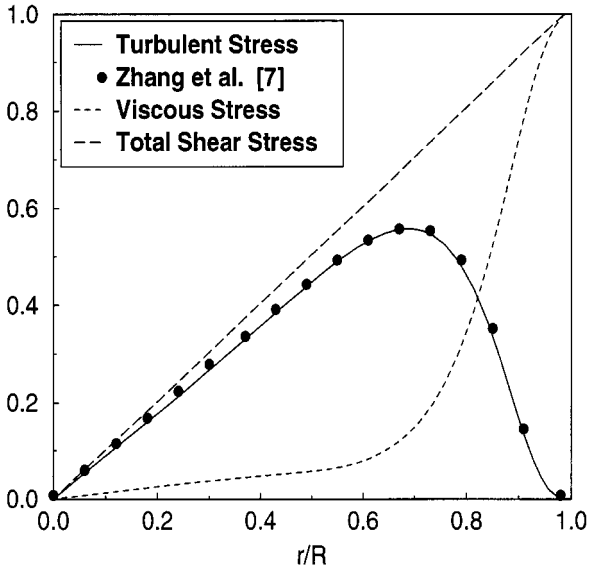

FIG. 9. Shear stresses.

between the computations is generally good; also, the limiting values in the near wall region are consistent with the theoretical ones, obtained from physical considerations on the no-slip boundary condition and the continuity equation. No experimental data are available at this Reynolds number. The Reynolds shear stresses and the viscous one are shown in Fig. 9, together with the data of [7], which have been normalized with the theoretical value of the shear velocity. The total shear stress distribution is linear for fully developed pipe flows, since it must balance the imposed volumetric flow rate. The Reynolds stress attains its maximum value at $r/R \approx 0.68,\ r^+ \approx 30$, before decaying rapidly to zero at the wall where the viscous shear stresses are predominant.

In Fig. 10 we give the instantaneous distributions of the three Cartesian components of the vorticity along a line crossing the pipe center in the $r - z$ plane. Note that although the

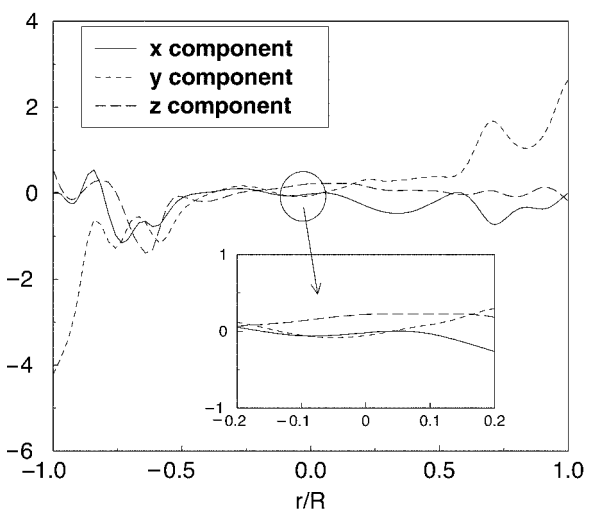

FIG. 10. Vorticity profiles.

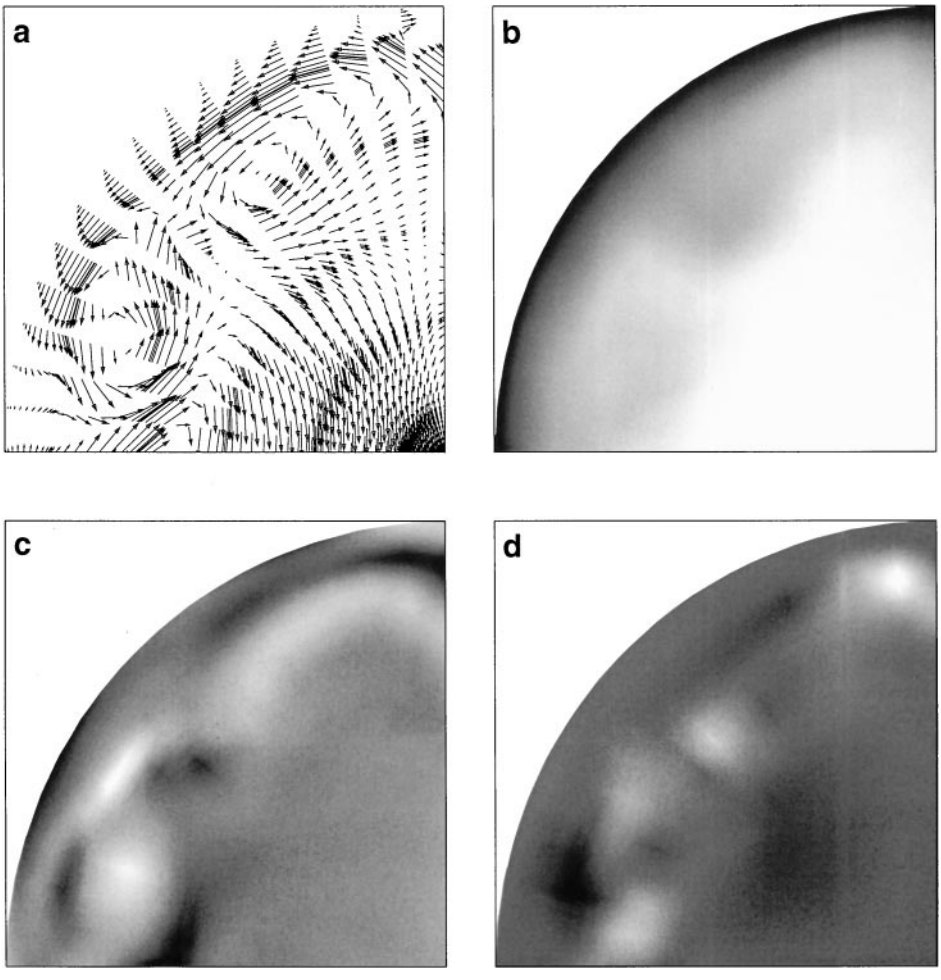

FIG. 11. Instantaneous velocity vectors (a), streamwise velocity u (b), streamwise vorticity ω_z (c), and shear stress uv (d).

continuity of the gradient of the velocity field is not explicitly enforced at the interfaces, the vorticity components are smooth and perfectly resolved in the whole domain. With reference to the pipe axis the same figure shows a close up view in the core region which clearly demonstrates the effectiveness of the treatment of the singularity. In Fig. 11 we present the velocity vectors, the streamwise velocity, the streamwise vorticity, and the shear stress uv taken from an instantaneous field. Let us focus the attention on the large scale coherent structures of Fig. 11a. The two pairs of co-rotating vortices associated with the two mushroom-type structures are clearly visible in Fig. 11b. The streamwise vorticity of Fig. 11c also shows a peak at similar locations. Finally Fig. 11d indicates that the Reynolds stress generation (light area) is predominant in the near wall region. In particular the top right maximum seems to be associated with a fourth quadrant event (sweep), that is, positive streamwise fluctuations are connected with high speed fluid lumps arriving at the wall. All instantaneous quantities appear smooth and well resolved.

5. CONCLUSION

In this paper we have discussed the construction of a fast pseudo-spectral Navier–Stokes solver for cylindrical geometries which is shown to possess the accuracy required for the direct numerical simulation of turbulent flows with two homogeneous directions. The formulation overcomes the issues related to the axis singularity adopting as expansion basis in the radial direction standard Chebyshev polynomials combined with a special set of collocation nodes. The multi-domain technique based on patching interfaces provides additional flexibility both in terms of computational efficiency and near wall resolution, the latter being a key issue for the simulation of turbulent flows. The elliptic kernel enjoys the efficiency of an analytic expansion of the harmonic extension. We have demonstrated that whole scheme attains exponential accuracy on a domain basis not only for elliptic model problems, but also for the full Navier–Stokes equations.

ACKNOWLEDGMENTS

The authors express their gratitude to Professor R. Vaccaro, director of the IRSIP (Istituto Ricerche e Sistemi Informatici Paralleli, CNR, Napoli, Italy), who kindly supported and provided computational resources to this work.

REFERENCES

1. C. Canuto, M. Y. Hussaini, A. Quarteroni, and T. A. Zang, *Spectral Methods in Fluid Dynamics* (Springer–Verlag, New York/Berlin, 1988).
2. *Spectral Methods for Flow Simulation*, Lecture Series Monographs (von Karman Institute for Fluid Dynamics, 1994).
3. S. A. Orszag and A. T. Patera, Secondary instability of wall bounded shear flows, *J. Fluid Mech.* **128**, 347 (1983).
4. A. Leonard and A. Wray, A new numerical method for the simulation of three dimensional flow in a pipe, in *8th International Conference on Numerical Methods in Fluids* (Springer–Verlag, New York/Berlin, 1982), Vol. 170, p. 335.
5. V. G. Priymak, Pseudospectral algorithms for Navier–Stokes simulation of turbulent flows in cylindrical geometry with coordinate singularities, *J. Comput. Phys.* **118**, 366 (1995).
6. A. T. Patera, A spectral element method for fluid dynamics: Laminar flow in a channel expansion, *J. Comput. Phys.* **54**, 468 (1984).
7. Y. Zhang, A. Gandhi, A. G. Tomboulides, and S. A. Orszag, Simulation of pipe flow, in *Application of Direct and Large Eddy Simulation to Transition and Turbulence* (AGARD, 1994).
8. R. D. Henderson and G. E. Karniadakis, Unstructured spectral element methods for simulation of turbulent flows, *J. Comput. Phys.* **122**, 191 (1995).
9. J. Van Kan, A second order accurate pressure correction scheme for viscous incompressible flow, *J. Sci. Stat. Comput.* **7**, 870 (1986).
10. A. Quarteroni and A. Valli, *Numerical Approximation of Partial Differential Equations* (Springer–Verlag, New York/Berlin, 1994).
11. P. J. Davis and P. Rabinowitz, *Methods of Numerical Integration* (Academic Press, Orlando, 1984).
12. S. A. Orszag, Spectral methods for problems in complex geometries, *J. Comput. Phys.* **37**, 70 (1980).
13. D. Funaro, Domain decomposition methods for pseudo-spectral approximation. Part I. Second order equations in one dimension, *Numer. Math.* **52**, 329 (1988).
14. A. Y. Aydemir and D. C. Barnes, Three-dimensional nonlinear incompressible MHD calculations, *J. Comput. Phys.* **53**, 100 (1984).

15. L. S. Tuckerman, Divergence free velocity fields in non-periodic geometries, *J. Comput. Phys.* **80**, 403 (1989).
16. D. Schnack and J. Killeen, Nonlinear, two-dimensional magnetohydrodynamic calculations, *J. Comput. Phys.* **35**, 110 (1980).
17. S. A. Orszag, Fourier series on spheres, *Monthly Weather Rev.* **102**, 56 (1974).
18. S. Chandrasekhar, *Hydrodynamic and Hydromagnetic Stability* (Dover, New York, 1981).
19. P. S. Marcus, Simulation of Taylor–Couette flow. Part. 1. Numerical methods and comparison with experiment, *J. Fluid Mech.* **146**, 45 (1984).
20. P. S. Marcus, Simulation of Taylor–Couette flow. Part. 2. Numerical results for wavy-vortex flow with one travelling wave, *J. Fluid Mech.* **146**, 65 (1984).
21. J. G. M. Eggels, F. Unger, M. H. Weiss, J. Westerweel, R. J. Adrian, R. Friedrich, and F. T. M. Nieuwstadt, Fully developed turbulent pipe flow: A comparison between direct numerical simulation and experiment, *J. Fluid Mech.* **268**, 175 (1994).
22. J. Kim, P. Moin, and R. Moser, Turbulence statistics in fully developed channel flow at low Reynolds number, *J. Fluid Mech.* **177**, 133 (1987).
23. R. A. Antonia, M. Teitel, J. Kim, and L. W. B. Browne, Low Reynolds number effects in a fully developed turbulent channel flow, *J. Fluid Mech.* **236**, 579 (1992).
24. V. C. Patel and M. R. Head, Some observations on skin friction and velocity profiles in fully developed pipe and channel flows, *J. Fluid Mech.* **38**, 181 (1969).